PHYSICAL REVIEW APPLIED **15,** 064026 (2021)

Editors' Suggestion

Charge-Collection Efficiency in Back-Illuminated Charge-Coupled Devices

Guillermo Fernandez Moroni,[1,*] Kevin Andersson,[2,1,†] Ana Botti,[2,‡] Juan Estrada,[1,§] Dario Rodrigues,[2,1,¶] and Javier Tiffenberg[1,‖]

[1] *Fermi National Accelerator Laboratory, P.O. Box 500 Batavia, Illinois 60510, USA*

[2] *Department of Physics, FCEN, University of Buenos Aires and IFIBA, CONICET, CP1428 Buenos Aires, Argentina*

(Received 13 July 2020; revised 3 February 2021; accepted 17 May 2021; published 10 June 2021)

Low-noise fully depleted charge-coupled devices have been identified as a unique tool for dark-matter searches, low-energy neutrino physics, and x-ray detection. The charge-collection efficiency (CCE) for these detectors is a critical performance parameter for current and future experiments. We present a technique to characterize the CCE in back-illuminated CCDs based on soft x rays. This technique is used to study two different detector designs. The results demonstrate the importance of the backside processing for the detection of charge packages near threshold, showing that a recombination layer of a few microns significantly distorts the low-energy spectrum. The studies demonstrate that the region of partial charge collection can be reduced to a thickness of less than 1 μm with adequate backside processing.

DOI: 10.1103/PhysRevApplied.15.064026

I. THICK FULLY DEPLETED CCDs FOR DM, NEUTRINO EXPERIMENTS, AND X-RAY DETECTION

Charge-coupled devices (CCDs) with low readout noise and large active volume have been identified among the most promising detector technologies for the low-mass direct dark-matter (DM) search experiments, probing electron and nuclear recoils from sub-giga-electronvolt DM [1–5]. The recent development of the skipper CCD [6,7] has demonstrated the ability to measure ionization events with subelectron noise, extending the reach of this technology to unprecedented low energies. Experiments based on this technology are planned for the coming years with active masses going from 100 g to several kilograms [8,9]. At the same time, the low-noise CCD technology has been implemented in low-energy neutrino experiments [10,11] and its use is planned for future developments [12]. Back-illuminated CCDs are also broadly used as soft x-ray detectors in space-based x-ray telescopes [13–16] and ground-based instruments associated with advanced light sources [17].

There are several key performance parameters for the CCD sensors to be used in future instruments that are part of a significant R&D effort for future projects [8,9,12]. The most important performance requirements are the pixel dark current [7], readout-noise optimization [18], and charge transport in the sensor [19].

The charge-collection efficiency (CCE) is defined as the fraction of the total charge produced during an ionization event that is collected in the CCD pixel for later readout.

The electric field required to fully deplete a silicon volume is related to the dopant concentration and the temperature of the sensor [20]. When the strength of the electric field is not enough to reach this condition, recombination can occur, as the electron-hole pair lifetime becomes smaller than the amount of time that it spends on the undepleted region [21]. While geminate recombination can occur at any applied voltage, this effect is beyond the scope of this paper and does not affect the results.

In the backside of CCDs, the dopant concentration can be nonuniform and can have a large gradient [20]. In the active volume of a fully depleted detector, the CCE is approximately 100% but in regions with higher dopant concentration, the reduced mobility, lifetime, and local electric field experienced by the charge carriers can lead to recombination [22]. In these regions, the CCE could be less than 100%. The quantitative measurement of this effect is the goal of this work. Regions of partial CCE distort the measured spectrum of ionization events, affecting energy calibration and particle identification.

Back-illuminated CCDs in astronomy are treated to have a thin entrance window for light, with low reflectivity. This is especially important when detectors are used for wavelengths shorter than 500 nm [23–25]. The measurements presented in Ref. [26] compare the detection efficiency for visible photons with the reflectivity. These studies show

*gfmoroni@fnal.gov
†kevinandersson456@gmail.com
‡abotti@df.uba.ar
§estrada@fnal.gov
¶rodriguesfm@df.uba.ar
‖javiert@fnal.gov

that all photons with wavelengths (absorption lengths) between 650 nm (3.6 μm and 850 nm 18.7 μm) are fully detected unless they are reflected on the back surface. These results suggest that the bulk of the detector has 100% CCE and that any recombination on these sensors occurs only on the first few microns near the back surface.

For thick CCDs, such as those used in DM [1–7] and neutrino experiments [10,11], a backside Ohmic contact is required to apply the needed substrate bias to fully deplete the sensor [20]. At the same time, different processing techniques are used on the backside to reduce the dark current. The backside processing of these sensors determines the field shaping near the surface and has a large impact on the CCE for events in that region. Here, we study the CCE for back-illuminated detectors with a thickness of more than 200 μm.

II. DETERMINATION OF THE BACKSIDE CCE USING X RAYS

X rays can be used to characterize the CCE near the back surface of a CCD. In Fig. 1, we provide a schematic view of our x-ray experimental setup together with the critical variables used in this analysis. Below, we list important aspects and definitions used in this work:

(a) The x-ray source is placed facing the backside of the device. Photons reaching the sensor are broadly distributed over a large area of the array. The geometry of the source and relative position to the device determine the incident angle of the x ray. $h(\theta)$ is the probability density function (PDF) of possible incident angles θ of photons in the region of interest in the detector (where θ is the angle between the sensor normal and the photon, as depicted in Fig. 1). $h(\theta)$ can be evaluated numerically using a simple toy Monte Carlo (MC) simulation that reflects the geometry of the experimental setup. This toy MC does not simulate particle interactions, as its goal is to provide the intensity and incident angle of the x rays. We compare the $h(\theta)$ obtained this way with another obtained from a detailed GEANT4 simulation (see Sec. III A) and find excellent agreement between them.

(b) The x-ray photons can reach the partial charge collection (PCC) layer and the bulk of the sensor volume. They will mainly interact by photoelectric absorption following an exponential distribution in the amount of material traversed. The depth of the interaction in the silicon also depends on the incident angle θ. The joint PDF governing the incident angle and depth of interaction is $g'(z,\ \theta) = \exp\{-z/[\lambda\cos(\theta)]\}h(\theta)/[\lambda\cos(\theta)]$ for $z \geq 0$ $[g'(z,\ \theta) = 0$ for $z < 0]$, where z is the depth in the silicon measured from the back of the sensor and λ is the attenuation length of the photon. The sensor position relative to the source defines the expected maximum and minimum incident angles (θ_1 and θ_2, respectively) of the photons. These limits are used to calculate the marginal PDF of the interaction depth in the sensor:

$$g(z) = \int_{\theta_1}^{\theta_2} g'(z,\theta)d\theta. \quad (1)$$

(c) X rays produce ionization events with a charge mean value $q_i = E_i/\epsilon$, where E_i is the energy of the photon and $\epsilon = 3.75$ eV is the mean ionizing energy [27]. We assume that the initial charge packet for all photoelectric absorption events is given by a Gaussian distribution with a mean equal to the x-ray energy and a width given by the Fano fluctuations [27]. The primary charge ionization is the same for the PCC layer and the bulk of the sensor, as represented in Fig. 1.

(d) $\varepsilon(z)$ is the CCE function in the backside of the detector. The function indicates the fraction of carriers that are collected by the pixel after drifting away from the PCC layer (carriers that do not recombine in the PCC layer). This function depends on the depth of the interaction. If the primary interaction occurs closer to the back of the CCD (further away from the bulk of the sensor), carriers will have more options to recombine before they reach the bulk. Thus, $\varepsilon(z)$ increases monotonically.

(e) q_f is the charge that escapes from the PCC layer and can be collected and recorded by the sensor. As illustrated in Fig. 1, this will depend on the interaction depth of the photon. The PDF governing the distribution of possible values of q_f is called $f(q_f)$, which is the measurable differential spectrum from the output images of the detector. This distribution includes the fluctuations that are

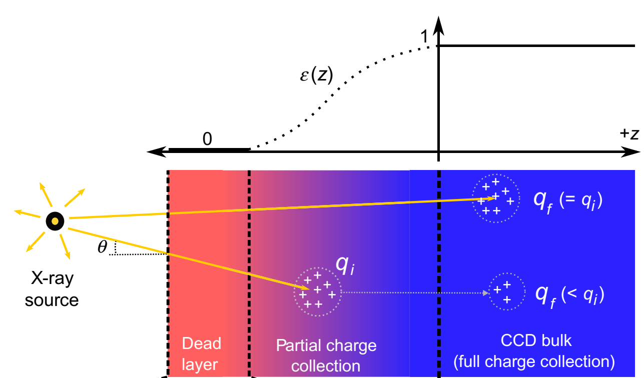

Unthinned CCD-A	2.2-μm SiO_2	Unk. (this work) Si	~670-μm Si
Thinned CCD-B	0.1 + 0.04 + 0.02 μm SiO_2+ZrO_2+In	Unk. (this work) Si	~200-μm Si

FIG. 1. A sketch of the CCD back illumination with an x-ray source. The photon penetrates the CCD, producing a cloud of charge q_i, the fraction $\varepsilon(z)$ of this charge that is collected depending on the depth z. The region near the back of the CCD where $0 < \varepsilon(z) < 1$ is the PCC layer. The shape of $\varepsilon(z)$ is arbitrary for purposes of illustration. Unk; Unknown.

produced by the readout noise of the detector, which are typically Gaussian for scientific CCDs [21].

From the previous definitions, the measured charge can be expressed as

$$q_f = q_i \varepsilon(z), \tag{2}$$

where the measured charge q_f is a function of the produced charge, q_i, and the charge production depth, z. For events that are produced deep in the CCD, $\varepsilon = 1$ and $q_f = q_i$ (Fig. 1).

A. Determination of the efficiency function using a monochromatic x-ray source

From Eq. (2) and due to the monotonically increasing $\varepsilon(z)$, there is a one-to-one relationship between the final collected charge of a photon and its interaction depth in the PCC layer for the case of a monoenergetic x-ray source. Any measured event with a charge packet smaller than q_i carries information about the efficiency function. Then, there is a one-to-one relationship between the cumulative distribution function (CDF) of the measured spectrum [$F(q_f)$] and the CDF of the interaction depth [$G(z)$]

$$F(q_f) = \int_0^{q_f} f(x)dx = \int_0^{z} g(x)dx = G(z), \tag{3}$$

where $f(x)$ is the measured spectrum and z is such that $\varepsilon(z) = q_f/q_i$.

Because the measurements at low charge values can be affected by readout noise, it is experimentally useful to use the complement of the CDF: integrating from the energy of the x-ray peak in the direction of low charge values. This reduces the systematic uncertainties related to the modeling of the readout noise at low signal levels. In this case, Eq. (3) can be rewritten as

$$1 - F(q_f) = \int_{q_f}^{q_i} f(x)dx = \int_{z}^{\infty} g(x)dx = 1 - G(z). \tag{4}$$

Then, the method consists of finding z for each q_f such that $1 - G(z) = 1 - F(q_f)$. Then, for each $(z,\ q_f)$ pair, the efficiency function is $\varepsilon(z) = q_f/q_i$.

The method to calculate the CCE using a monochromatic x-ray peak is summarized in Table II of the Appendix. Partial charge depositions by secondary low-probability x-ray interaction in the bulk of the sensor could add systematic errors to the previous method. Its contribution depends on the setup geometry and the sensor dimensions and materials. In Sec. III, we discuss the impact of these effects using a detailed GEANT4 simulation.

It is also possible to work directly with the PDF instead of the CDF but this approach is numerically harder and requires assumptions on the shape of $\varepsilon(z)$ to be solvable.

B. Determination of the efficiency function using an ^{55}Fe source

^{55}Fe X-ray sources are broadly used in the calibration of CCDs and for the characterization of their performance [21]. In this paper, we extend their use to the characterization of the CCE in the PCC layer using the methodology proposed in Sec. II A. The main characteristics of the x rays emitted by ^{55}Fe are summarized in Table I. The two K_α lines have similar energies and attenuation lengths and can be treated as a single monoenergetic x-ray line for this analysis.

In this case, the joint PDFs for the interaction depth ($z \geq 0$) and incident angle are

$$g'_\alpha(z,\theta) = \exp\{-z/[\cos(\theta)\lambda_\alpha]\}h(\theta)/[\cos(\theta)\lambda_\alpha] \tag{5}$$

and

$$g'_\beta(z,\theta) = \exp\{-z/[\cos(\theta)\lambda_\beta]\}h(\theta)/[\cos(\theta)\lambda_\beta] \tag{6}$$

for the X_{K_α} and X_{K_β}, respectively. λ_α and λ_β are the attenuation lengths for each photon from Table I. The angular distribution is the same in both cases. $g'_\alpha(z,\theta) = g'_\beta(z,\theta) = 0$ for $z < 0$.

The CDF of the measured spectrum can be expressed as

$$F(q_f) = p_\alpha F_\alpha(q_f) + p_\beta F_\beta(q_f), \tag{7}$$

where F_α and F_β are the CDFs of the spectrum of events for each photon and p_α and p_β are the relative intensities

TABLE I. The ^{55}Fe x-ray energies, the mean *e-h* pair production (using the mean ionization energy), the relative intensity, and the attenuation length in microns [28].

X_K	E (keV)	Mean *e-h* pair production, q_i	Relative intensity	Attenuation length, λ
α_2	5887.65	1570	0.297 (5)	28.7
α_1	5898.75	1573	0.583 (10)	28.9
β_3	6490.45	1731	0.120 (2)	38.0

X_K; Spectral line denomination.

given in Table I normalized by the number of disintegrations. Generalizing Eq. (3)

$$F_\alpha(q_f) = G_\alpha(z_\alpha) \quad \text{and} \quad F_\beta(q_f) = G_\beta(z_\beta), \tag{8}$$

where G_α and G_β are the CDFs of the interaction depth of the X_{K_α} and X_{K_β}, respectively. They are obtained after integrating the PDF in Eqs. (5) and (6) over all the possible values of θ [as in Eq. (1)]. z_α and z_β are interaction depths such that $\varepsilon(z_\alpha) = q_f/q_{i,\alpha}$ and $\varepsilon(z_\beta) = q_f/q_{i,\beta}$ where $q_{i,\beta}$ and $q_{i,\beta}$ are the expected numbers of electron-hole pairs produced by the X_{K_α} and X_{K_β} photons from Table I. Since we assume a monotonically increasing $\varepsilon(z)$ function, then $z_\alpha \geq z_\beta$. Replacing Eqs. (8) in (7),

$$F(q_f) = p_\alpha G_\alpha(z_\alpha) + p_\beta G_\beta(z_\beta), \quad \text{with } z_\alpha \geq z_\beta. \tag{9}$$

A recursive nonlinear numeric solver can be used to find the z_α and z_β that solve this equation in an iterative way. We start with an ansatz for the CCE function, $\varepsilon_0(z)$, from which we obtain $z_{\beta,0}$ as a function of $z_{\alpha,0}$ using $q_f = q_{i,\alpha}\varepsilon_0(z_{\alpha,0}) = q_{i,\beta}\varepsilon_0(z_{\beta,0})$. Then, the right-hand side of Eq. (9) can be rewritten as a function of $z_{\alpha,0}$ only and numerically solved [as Eq. (4)] to obtain an instance of the CCE function: $\varepsilon_1(z)$. Using $\varepsilon_1(z)$ as the ansatz, this process can be repeated until the difference between the CCE function obtained from Eq. (9) and the ansatz is smaller than the required accuracy.

Although the procedure described above is required to obtain the most precise measurement of $\varepsilon(z)$, three features of the ^{55}Fe source can be used to greatly simplify the problem when an approximately 10% error is acceptable:

(a) A larger number of K_α than K_β photons, since $p_\alpha/p_\beta = 7.33$
(b) $G_\alpha(z_\alpha)$ and $G_\beta(z_\beta)$ are continuous and similar
(c) $q_{i,\beta}$ and $q_{i,\alpha}$ differ only by 10%

As the interactions in the PCC layer are dominated by the K_α photons (7.33 times more intense), only a small contribution is introduced by the photons from the K_β peak. The treatment of Eq. (9) can be greatly simplified by the approximation $z_{\text{eff}} = z_\alpha = z_\beta$, where z_{eff} is an effective interaction-depth value that will be between the true z_α and z_β. Under this approximation, a rough estimate of the error can be obtained by computing ε under two extreme assumptions for the initial charge package:

(1) $\varepsilon_{\text{high}}(z_{\text{eff}}) = q_f/q_{i,\alpha}$
(2) $\varepsilon_{\text{low}}(z_{\text{eff}}) = q_f/q_{i,\beta}$

The difference between them is smaller than 10% and the true value for ε lies between these two extreme cases. If we use a more realistic effective value, q_{eff}, for the initial charge packet,

$$q_{\text{eff}} = p_\alpha q_{i,\alpha} + p_\beta q_{i,\beta}, \tag{10}$$

the CCE function that is obtained is almost identical to the one resulting from the iterative "exact" solution of Eq. (9).

A summary of the proposed method to evaluate the PCC layer using an ^{55}Fe source is provided in Table III, in the Appendix.

III. EXPERIMENTAL RESULTS

Here, we study two CCDs with different backside treatments.

CCD-A is designed by the LBNL Microsystems Laboratory (MSL) [29] and fabricated at Teledyne-DALSA as part of the R&D effort for low-energy neutrino experiments [10] and low mass direct DM search [3]. This is a rectangular CCD with 8 million square pixels of 15 μm × 15 μm each. The CCD is fabricated in *n*-type substrate with a full thickness of 675 μm. The resistivity of the substrate is greater than 10 000 Ω cm. The CCD is operated with a 40-V bias voltage that fully depletes the high-resistivity substrate, using the method developed in Ref. [20]. To trap impurities that migrate during the sensor processing, a 1 μm thick *in situ* doped polysilicon (ISDP) layer is deposited on the backside of the detector. This layer plays a critical role in controlling the dark current of the detector. Additional layers of silicon nitride, phosphorous-doped polysilicon, and silicon dioxide are added to the backside (2 μm total thickness). Phosphorous can migrate into the high-resistivity material, producing a region of a few microns where charge can recombine before drifting to the collecting gates of the detector. This region constitutes the PCC layer that we characterize with ^{55}Fe x rays, as shown in Fig. 1.

CCD-B is also designed by the MSL and fabricated in high-resistivity *n*-type silicon at Teledyne-DALSA, using the same process as for CCD-A with a few important differences: the detector has 4 million 15 μm × 15 μm pixels and a thickness of 200 μm. The backside of the sensor is processed for astronomical imaging, using a technique developed at the MSL [20], to improve the sensitivity to blue light. A backside Ohmic contact is formed by low-pressure chemical-vapor-deposition ISDP. This layer is made thin, typically 10–20 nm, to minimize the absorption of blue photons and is robust to the overdepleted operation that is necessary to guarantee full depletion across the entire CCD. This detector is operated at a bias voltage of 40 V. Because of its backside treatment, this detector is not expected to have significant charge recombination near the back surface. The detector is exposed to ^{55}Fe x rays on the backside, as shown in Fig. 1.

We use a standard ^{55}Fe calibration source encapsulated in stainless steel. Its active area is covered by a circular beryllium window that is 0.25 mm thick and 5 mm in diameter. The active ^{55}Fe foil is 1 μm thick and is deposited on a nickel backing. It is located 3.55 cm away from the CCDs. As the events produced in the PCC region may show a nonstandard shape, we do not use any quality cuts related to the shape of the events. To avoid edge-related effects, only events 50 pixels away from the edge of the sensor are considered in the analysis.

The effective depth distribution of interacting photons is calculated using a toy MC simulation. After inspecting its functional form, we find that it can be accurately parametrized by the sum of two independent exponential functions:

$$G(z) = \tilde{I}_\alpha \exp(-z/\tilde{\tau}_\alpha) + \tilde{I}_\beta \exp(-z/\tilde{\tau}_\beta), \qquad (11)$$

where $\tilde{I}_\alpha(\tilde{I}_\beta)$ and $\tilde{\tau}_\alpha(\tilde{\tau}_\beta)$ are obtained by fitting the PDF produced from the MC simulation and represents the effective relative intensity and optical depth for the $\alpha(\beta)$ spectral line after the angular distribution of the photons is taken into account. For the geometry of our experimental setup, we obtain $\tilde{I}_\alpha = 0.034$, $\tilde{I}_\beta = 0.0032$, $\tilde{\tau}_\alpha = 25.74$ μm, and $\tilde{\tau}_\beta = 37.19$ μm. The effect of the passive materials on the calculation of angular distribution of photons reaching the active volume is found to be negligible for this analysis. The active area of the ^{55}Fe is used in the simulations.

A. Results for CCD-A

The spectrum of measured charge for CCD-A is shown in the left-hand panel of Fig. 2 and is compared with a detailed GEANT4 [30] simulation assuming perfect CCE for the entire volume of the sensor [$\varepsilon(z) = 1$]. This simulation computes the contribution to the spectrum that comes from multiple scattering events in the dead layer, the Compton interactions, and other processes with low probability such as fluorescence. This simulation accounts for the possibility of electrons leaving the CCD and producing a partial energy-deposition event. As the direction of the electron is highly correlated with the direction of the incoming x ray, only a small fraction leave the CCD. Our simulation also includes the possibility of kiloelectronvolt-scale photons leaving the sensor, producing an event with reduced reconstructed energy. The GEANT4 simulation geometry includes all accessories and support materials (including the vacuum vessel walls) that have a direct line of sight to the active area of the source. The source model includes the Ni backing material, the 1-μm active foil, and the 0.25-mm Be window. The layers shown in Fig. 1 are also included in the backside of the sensor. We also model the copper plates that are part of the package of the sensor. We do not include the stainless-steel screws (used to hold the copper package in place) or the flex cable that connects the sensor to the readout electronics. Their contribution is expected to be negligible, as there is no direct line of sight between them and the sensor. For the comparison of the simulated spectrum with the measured one, we include the Fano fluctuations [27] and the readout noise added in quadrature. The environmental background is measured to be below 2×10^{-5} in the scale of Fig. 2 and has a negligible contribution. The K_α and K_β peaks from Table I are evident. The excess of reconstructed events to the left of these peaks is attributed to the PCC layer, where charge recombination produces a measurement below the peak energy. The bumps in the simulation around 1100 e$^-$ and 1300 e$^-$ are the K_α and K_β escape peaks, respectively, as

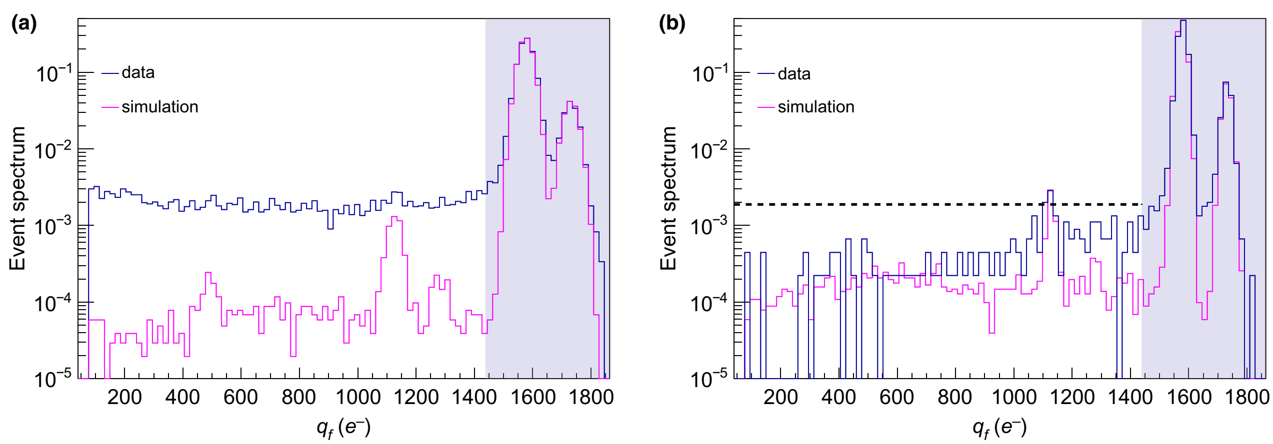

FIG. 2. The event spectra for CCD-A (left) and CCD-B (right) calculated using a bin size of 70 eV normalized by the number of measured events in the K_α peak: blue, measured spectra; magenta, simulated spectra of events from GEANT4. Left panel: spectra for CCD-A; 35 195 events in the histogram; 26 697 events in the K_α peak. Right panel: event spectra for CCD-B; 5452 events in the histogram; 4482 events in the K_α peak. The dashed black line indicates the expected level of events if the partial charge-collection layer on CCD-B is same as the one measured on CCD-A.

discussed in Ref. [31]. These peaks are expected to be suppressed in the measured data, because escape events are produced when a Si-fluorescence photon created in the interaction leaves the detector without being recorded. As the attenuation length in silicon for Si-fluorescence photons is approximately 10 μm, these escape events need to occur close to the surface of the sensor for the low-energy photons to have a large probability of leaving the detector. This region is the most affected by the energy-smearing effect produced by the PCC layer. Once the PCC is fully characterized, using the method described in this work, it is trivial to use the three-dimensional tracking information produced by the GEANT4 simulation to compute a simulated spectrum that includes the effect of the PCC layer (we use this technique as a self-consistency check). The peak at approximately 500 e^- in the simulated spectrum is produced by silicon fluorescence in the SiO_2 dead layer that covers the backside of the CCD. This peak is not expected to be visible in the measured spectrum, because most of the low-energy Si-fluorescence photons produced in the SiO_2 dead layer interact in the PCC layer before they can reach the region of full charge collection.

The data shown in Fig. 2 are used to measure the CCE function $\varepsilon(z)$, following the prescription in Sec. II B, and the results are shown in Fig. 3. The depth scale is chosen such that $\varepsilon(z = 0) = 0.9$. The shaded region corresponds to the energies between 5.4 keV and 7 keV, where the events from K_α and K_β are dominant and systematic uncertainties are expected to be important. In this region, the precise shape of the ε curve is less reliable.

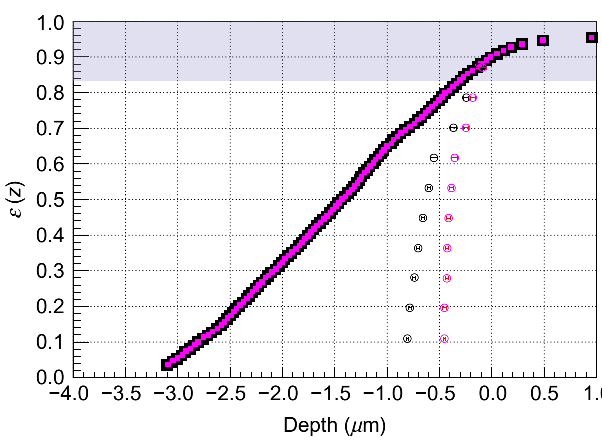

FIG. 3. The measured charge-collection efficiency for CCD-A (solid square markers) and CCD-B (open circle markers). The black points show the results without considering the background events predicted by the simulation. The magenta points show the results after correcting the experimental spectra by subtracting the background events from the simulations. The shaded area indicates the region where the detailed shape of the x-ray peaks affects the measurement, introducing more uncertainty.

B. Results for CCD-B

The spectrum of measured charge for CCD-B is shown in the right-hand panel of Fig. 2 and compared with a detailed GEANT4 simulation assuming perfect CCE. This simulation includes the contribution to the spectrum that comes from multiple scattering events in the dead antireflective layer, the Compton interactions, and other processes with low probability, such as fluorescence. In contrast to the results for CCD-A, the simulated spectrum of CCD-B can account for a significant fraction of the low-energy events and may play a role in the characterization of the PCC layer. For this reason, we compare results from use of the PENELOPE or LIVERMORE electromagnetic models included in GEANT4 and obtain statistically compatible simulated spectra. Although we recognize that there may be additional contributions to the low-energy spectrum, they would only reduce the number of candidate events produced in the PCC layer and thus further reduce the thickness of the PCC layer. To study this systematic, we are planning an experiment using lower-energy photons that will allow for a better precision on the measurement of thin PCC layers due to their smaller attenuation lengths.

As with CCD-A, the K_α and K_β spectral lines are evident. CCD-B has a different output stage that allows for a lower noise readout and produces higher-resolution peaks [6]. The relative rate of events on the left of the peaks is well below the rate observed for CCD-A and is consistent with the simulation. These events are produced mostly by low-probability Compton scattering of x rays. The environmental background for this CCD is below 1×10^{-7} in the scale of Fig. 2 and can be safely ignored for this analysis. The CCE function $\varepsilon(z)$ is determined as discussed in Sec. II B and the results are shown in Fig. 3. The measurement of $\varepsilon(z)$ is also performed after subtracting the predicted background from the GEANT4 simulation. As before, the horizontal axis is selected such that $\varepsilon(z = 0) = 0.9$.

IV. CONCLUSIONS

The results of CCD-A and CCD-B shown in Fig. 3 demonstrate the large impact that the backside processing has in the CCE for back-illuminated detectors. When a layer of a few microns with charge recombination is present on the CCD, the spectrum for low-energy x rays becomes significantly distorted. The charge recombination generates a significant number of lower-energy events in the spectrum. The backside processing performed in detectors optimized for astronomical instruments eliminates this issue for the most part, as shown with CCD-B. The backside treatment from CCD-B can be applied to thicker detectors. We plan to explore other techniques, as in Refs. [32,33]. The generation of low-energy events constitutes a major concern for experiments looking for rare signals near the detector threshold [1–7,10,11].

TABLE II. The methodology to calculate the PCC efficiency function using a monochromatic x-ray source.

(1) Calculate angular distribution of incident photons
Based on the geometry of the experiment, evaluate the angular distribution of incident photons reaching the region of interest in the sensor, $h(\theta)$.
(2) Calculate the depth distribution of events
Calculate $g'(z,\ \theta) = \exp\{-z/[\lambda\cos(\theta)]\}h(\theta)/[\cos(\theta)\lambda]$, $z > 0$.
Integrate this distribution over all possible values of θ to find the marginal PDF of the interaction depths $g(z)$ [follow Eq. (1)]. Then, find its CDF $G(z)$ [one can follow Eq. (3)].
(3) Make an spectrum of measured events
Calculate the spectrum of events reconstructed from the data and normalize it by the total number of events (N_T). This is the estimation $f(q_f)$.
(4) Calculate the CDF of the measured spectrum of events, $F(q_f)$.
Use Eq. (3).
(5) Find z
For a particular charge value q_f, find z that equals $F(q_f) = G(z)$.
This step can also be applied using the complement of the CDF to avoid systematic errors from noise models.
(6) Calculate the efficiency at z
$\varepsilon(z) = q_f/q_i$
(7) Repeat steps (4), (5), and (6) for a different q_f to complete $\varepsilon(z)$.

In this work, we introduce a technique to characterize the CCE in back-illuminated CCDs that can easily be generalized to other semiconductor detectors. The technique uses tools that are commonly available at detector-characterization laboratories. As shown here, the method is capable of measuring a PCC layer of a few micrometers even when a dead layer is present. The sensitivity to much thinner PCC layers is only limited by the energy of the ^{55}Fe x rays used. The technique can easily be extended for the measurement of much thinner recombination layers using lower-energy x rays. This technique is a powerful tool in the optimization of detectors for the next generation of low-threshold experiments looking for rare events such as DM or coherent neutrino-nucleus scattering [8,9,12]. This method can also be used for the characterization of back-illuminated CCD sensors used in space-based x-ray observatories such as *Hitomi* [13–15] or the upcoming X-Ray Imaging and Spectroscopy Mission (XRISM) [16].

The contribution of the PCC layer to low-energy events depends on the nature of the interacting background particle. Particles with a penetration range similar to the PCC-layer thickness produce larger contributions. The most recent results from the "Dark Matter in CCDs" (DAMIC) experiment [34] show that a significant portion of the low-energy events comes from this region and that they can be eliminated if the layer is narrowed.

TABLE III. The methodology to calculate the partial charge-collection efficiency function using an ^{55}Fe source.

(1) Calculate angular distribution of incident photons
Based on the geometry of the experiment, evaluate the angular distribution of incident photons reaching the region of interest in the sensor, $h(\theta)$.
(2) Calculate the depth distribution of events
Calculate $g'_\alpha(z,\ \theta)$ and $g'_\beta(z,\ \theta)$ for $z > 0$ from Eqs. (5) and (6), respectively. Integrate these distributions over all possible values of θ to find the marginal distributions of the interaction depths $g_\alpha(z)$ and $g_\beta(z)$ [follow Eq. (1)].
Then, find their CDF $G_\alpha(z)$ and $G_\beta(z)$ (one can follow Eq. (3)). Calculate the final CDF of the interaction depth $G(z) = p_\alpha G_\alpha(z) + p_\beta G_\beta(z)$.
(3) Make an spectrum of measured events
Calculate the spectrum of events reconstructed from the data and normalize it by total number of events (N_T). This is the estimation $f(q_f)$.
(4) Calculate the CDF of the measured spectrum of events, $F(q_f)$.
Use Eq. (3).
(5) Find z
For a particular charge value q_f, find z that equals $F(q_f) = G(z)$. This step can also be applied using the complement of the CDF to avoid systematic errors from noise models.
(6) Calculate the efficiency at z
$\varepsilon(z) = q_f/(p_\alpha q_{i,\alpha} + p_\beta q_{i,\beta})$
(7) Repeat steps (4), (5), and (6) for a different q_f to complete $\varepsilon(z)$.

ACKNOWLEDGMENTS

We thank the SiDet team at Fermilab for their support on the operations of CCDs and skipper CCDs, especially Kevin Kuk and Andrew Lathrop. This work was supported by Fermilab under DOE Contract No. DE-AC02-07CH11359. This manuscript has been authored by Fermi Research Alliance, LLC under Contract No. DE-AC02-07CH11359 with the U.S. Department of Energy, Office of Science, Office of High Energy Physics. The CCD development work was supported in part by the Director, Office of Science, of the U.S. Department of Energy under Contract No. DE-AC02-05CH11231. The U.S. Government retains and the publisher, by accepting the paper for publication, acknowledges that the U.S. Government retains a nonexclusive, paid-up, irrevocable, worldwide license to publish or reproduce the published form of this manuscript, or allow others to do so, for U.S. Government purposes.

APPENDIX: DETAILS OF THE METHOD

The details of the method to measure the CCE in the backside of a back-illuminated CCD are presented in Table II. The details of the method used with the ^{55}Fe source having two x-ray lines are presented in Table III.

[1] A. Aguilar-Arevalo, D. Amidei, X. Bertou, M. Butner, G. Cancelo, A. Castañeda Vázquez, B. A. Cervantes Vergara, A. E. Chavarria, C. R. Chavez, and J. R. T. de Mello Neto *et al.*, (DAMIC), Search for low-mass WIMPs in a 0.6 kg day exposure of the DAMIC experiment at SNOLAB, Phys. Rev. **D94**, 082006 (2016).

[2] A. Aguilar-Arevalo *et al.*, (DAMIC), First Direct-Detection Constraints on eV-Scale Hidden-Photon Dark Matter with DAMIC at SNOLAB, Phys. Rev. Lett. **118**, 141803 (2017).

[3] A. Aguilar-Arevalo *et al.*, (DAMIC), Constraints on Light Dark Matter Particles Interacting with Electrons from DAMIC at SNOLAB, Phys. Rev. Lett. **123**, 181802 (2019).

[4] M. Crisler, R. Essig, J. Estrada, G. Fernandez, J. Tiffenberg, M. Sofo haro, T. Volansky, and T.-T. Yu, (SENSEI), SENSEI: First Direct-Detection Constraints on Sub-GeV Dark Matter from a Surface Run, Phys. Rev. Lett. **121**, 061803 (2018).

[5] O. Abramoff *et al.*, (SENSEI), SENSEI: Direct-Detection Constraints on Sub-GeV Dark Matter from a Shallow Underground Run Using a Prototype Skipper-CCD, Phys. Rev. Lett. **122**, 161801 (2019).

[6] J. Tiffenberg, M. Sofo-Haro, A. Drlica-Wagner, R. Essig, Y. Guardincerri, S. Holland, T. Volansky, and T.-T. Yu, Single-Electron and Single-Photon Sensitivity with a Silicon Skipper CCD, Phys. Rev. Lett. **119**, 131802 (2017).

[7] L. Barak, I. M. Bloch, M. Cababie, G. Cancelo, L. Chaplinsky, F. Chierchie, M. Crisler, A. Drlica-Wagner, R. Essig, and J. Estrada *et al.*, SENSEI: Direct-Detection Results on Sub-GeV Dark Matter from a New Skipper-CCD, arXiv:2004.11378 (2020).

[8] M. Settimo, Search for low-mass dark matter with the DAMIC experiment, arXiv:2003.09497 (2020).

[9] The Oscura project is an R&D effort supported by the Department of Energy to develop a 10-kg skipper-CCD DM search.

[10] A. Aguilar-Arevalo, X. Bertou, C. Bonifazi, G. Cancelo, A. Castañeda, B. Cervantes Vergara, C. Chavez, J. C. D'Olivo, J. C. Dos Anjos, and J. Estrada *et al.*, (CONNIE Collaboration), Exploring low-energy neutrino physics with the coherent neutrino nucleus interaction experiment, Phys. Rev. D **100**, 092005 (2019).

[11] CONNIE Collaboration, A. Aguilar-Arevalo, X. Bertou, C. Bonifazi, G. Cancelo, B. A. Cervantes-Vergara, C. Chavez, J. C. D'Olivo, J. C. Dos Anjos, and J. Estrada *et al.*, Search for light mediators in the low-energy data of the CONNIE reactor neutrino experiment, J. High Energy Phys. **2020**, 54 (2020).

[12] The Violeta Collaboration is planning a kilogram-scale skipper-CCD experiment at a nuclear reactor facility.

[13] T. Takahashi, M. Kokubun, K. Mitsuda, R. L. Kelley, T. Ohashi, F. Aharonian, H. Akamatsu, F. Akimoto, S. W. Allen, and N. Anabuki *et al.*, *Hitomi* (ASTRO-H) x-ray astronomy satellite, J. Astron. Telesc. Instrum. Syst. **4**, 021402 (2018).

[14] M. J. L. Turner, A. Abbey, M. Arnaud, M. Balasini, M. Barbera, E. Belsole, P. J. Bennie, J. P. Bernard, G. F. Bignami, and M. Boer *et al.*, The European photon imaging camera on *XMM-Newton*: The MOS cameras, Astron. Astrophys. **365**, L27 (2001).

[15] K. Koyama, H. Tsunemi, T. Dotani, M. W. Bautz, K. Hayashida, T. G. Tsuru, H. Matsumoto, Y. Ogawara, G. R. Ricker, and J. Doty *et al.*, X-ray imaging spectrometer (XIS) on board Suzaku, Publ. Astron. Soc. Jpn **59**, 23 (2007).

[16] XRISM Science Team, Science with the X-Ray Imaging and Spectroscopy Mission (XRISM), arXiv:2003.04962 (2020).

[17] T. Hatsui and H. Graafsma, X-ray imaging detectors for synchrotron and XFEL sources, IUCrJ **2**, 371 (2015).

[18] G. Cancelo, C. Chavez, F. Chierchie, J. Estrada, G. Fernandez Moroni, E. E. Paolini, M. Sofo Haro, A. Soto, L. Stefanazzi, and J. Tiffenberg *et al.*, Low threshold acquisition controller for skipper CCDs, arXiv:2004.07599 (2020).

[19] M. Sofo Haro, G. Fernandez Moroni, and J. Tiffenberg, Studies on small charge packet transport in high-resistivity fully-depleted CCDs, arXiv:1906.11379 (2019).

[20] S. E. Holland, D. E. Groom, N. P. Palaio, R. J. Stover, and M. Wei, Fully depleted, back-illuminated charge-coupled devices fabricated on high-resistivity silicon, IEEE Trans. Electron Devices **50**, 225 (2003).

[21] J. R. Janesick, *Scientific Charge-Coupled Devices* (SPIE Press, Bellingham, Washington USA, 2001), Vol. 83.

[22] J. A. del Alamo and R. M. Swanson, Modelling of minority-carrier transport in heavily doped silicon emitters, Solid State Electron. **30**, 1127 (1987).

[23] S. Nikzad, M. E. Hoenk, P. J. Grunthaner, R. W. Terhune, F. J. Grunthaner, R. Winzenread, M. M. Fattahi, H.-F. Tseng, and M. P. Lesser, in *Proceedings of the SPIE*, Society of Photo-Optical Instrumentation Engineers (SPIE)

Conference Series, edited by D. L. Crawford and E. R. Craine (1994), Vol. 2198, p. 907.

[24] E. T. Hamden, A. D. Jewell, C. A. Shapiro, S. R. Cheng, T. M. Goodsall, J. Hennessy, M. Hoenk, T. Jones, S. Gordon, and H. R. Ong *et al.*, Charge-coupled devices detectors with high quantum efficiency at UV wavelengths, J. Astron. Telesc. Instrum. Syst. **2**, 036003 (2016).

[25] C. J. Bebek, J. H. Emes, D. E. Groom, S. Haque, S. E. Holland, P. N. Jelinsky, A. Karcher, W. F. Kolbe, J. S. Lee, and N. P. Palaio *et al.*, Status of the CCD development for the dark energy spectroscopic instrument, J. Instrum. **12**, C04018 (2017).

[26] M. H. Fabricius, C. J. Bebek, D. E. Groom, A. Karcher, and N. A. Roe, in *Proceedings of the SPIE*, Society of Photo-Optical Instrumentation Engineers (SPIE) Conference Series, edited by M. M. Blouke (2006), Vol. 6068, p. 144.

[27] D. Rodrigues, K. Andersson, M. Cababie, A. Donadon, A. Botti, G. Cancelo, J. Estrada, G. Fernandez-Moroni, R. Piegaia, and M. Senger *et al.*, Absolute measurement of the Fano factor using a skipper-CCD, arXiv:2004.11499 (2020).

[28] M.-M. Bé, V. Chisté, C. Dulieu, E. Browne, C. Baglin, V. Chechev, N. Kuzmenko, R. Helmer, F. Kondev, and D. MacMahon *et al.*, *Table of Radionuclides*, Monographie BIPM-5, Vol. 3 (Bureau International des Poids et Mesures, Pavillon de Breteuil, F-92310 Sèvres, France, 2006).

[29] Https://engineering.lbl.gov/microsystems-laboratory/.

[30] Https://geant4.web.cern.ch.

[31] J. Jaeckel and S. Roy, Spectroscopy as a test of Coulomb's law: A probe of the hidden sector, Phys. Rev. **D82**, 125020 (2010).

[32] Q. Looker, B. Aguirre, M. Hoenk, A. Jewell, M. Sanchez, and B. Tierney, Superlattice-enhanced silicon soft x-ray and charged particle detectors with nanosecond time response, Nucl. Instrum. Methods Phys. Res. Sec. A: Accelerators Spectrometers Detectors Associated Equip. **916**, 148 (2019).

[33] J. Blacksberg, S. Nikzad, M. E. Hoenk, S. E. Holland, and W. F. Kolbe, Near-100 silicon imagers, IEEE Trans. Electron Devices **55**, 3402 (2008).

[34] R. Catena and P. Ullio, Results on low-mass weakly interacting massive particles from a 11 kg-day target exposure of DAMIC at SNOLAB, arXiv:2007.15622 [astro-ph.CO] (2020).